MNRAS **000**, 1–17 (2020) Preprint 13 October 2020 Compiled using MNRAS LATEX style file v3.0

RZ Mic: Identified modes in an Algol-type eclipsing binary with a δ Sct component

Margaret Streamer[1]★, Michael J. Ireland[1], Meridith Joyce[1,4] Simon J. Murphy[2,3], and Maruša Žerjal[1]

[1] *Research School of Astronomy and Astrophysics, Australian National University, Canberra, ACT, 2611, Australia*
[2] *Sydney Institute for Astronomy (SIfA), School of Physics, The University of Sydney, NSW 2006, Australia*
[3] *Stellar Astrophysics Centre, Department of Physics and Astronomy, Aarhus University, DK-8000 Aarhus C, Denmark*
[4] *ARC Centre of Excellence for All Sky Astrophysics in 3 Dimensions (ASTRO 3D), Australia*

Accepted XXX. Received YYY; in original form ZZZ

ABSTRACT

Our aim was to identify the δ Sct-type pulsation modes observed in the RZ Mic binary system to determine if such binary systems are candidates for identifying pulsation modes and hence the fundamental parameters of a cohort of single stars with similar frequency patterns and low rotational velocities ($\leq 50\,\mathrm{km\,s^{-1}}$). We used photometry from *TESS* and three ground-based bands (B, V and I) in addition to spectroscopy that resolved the velocities of the two components. We derived the fundamental parameters of both stars of the RZ Mic system which was modelled as a semi-detached, Algol-type binary with a δ Sct star component. The primary star was the pulsator with a mass of $2.18 \pm 0.10\,M_{\odot}$, radius of $2.43 \pm 0.05\,R_{\odot}$ and $T_{\rm eff}$ of 7300^{+200}_{-100} K. The secondary star was a sub-giant which had filled its Roche lobe. Its mass was $0.57 \pm 0.02\,M_{\odot}$, radius = $3.97\,R_{\odot}$ and $T_{\rm eff} = 4373 \pm 100$ K. We identified only three significant frequencies in the δ Sct star, two of which were also seen in the ground-based B and V data. The dominant peak, f_1, at $13.522\,\mathrm{d^{-1}}$ had an amplitude of 10.863 mmag. We identified the modes of all three observed frequencies by modelling the evolution of a single star which matched our dynamically-derived mass, radius and $T_{\rm eff}$ for the pulsator, but only after enhancing its metallicity to greater than solar values. The highest-amplitude frequency of $13.522\,\mathrm{d^{-1}}$ was identified as a mixed mode, $n = 1$, $l = 1$, $m = -1$. Mode identification was only possible because of the combination of a strong density-constraint afforded by the binary modelling and tidal-locking in the binary system from which the rotation rate of the pulsator was known.

Key words: variables: δ Sct– binaries: eclipsing – asteroseismology

1 INTRODUCTION

Delta Scuti (δ Sct) stars are classified as p mode, pulsating A- to F- stars found at the base of the instability strip on the HR diagram. In principle, their internal structure and parameters, including age, should be discernible from their pulsation modes. Despite the vast amounts of exquisite, high-cadence, continuous data over substantial time periods from space-based observatories, such as *Kepler* (Borucki et al. 2010), *CoRoT* (Auvergne et al. 2009) and the Transiting Exoplanet Survey Satellite, *TESS* (Ricker et al. 2015) which have revolutionised the studies of δ Sct stars, precise stellar parameters of single stars remain difficult to ascertain and rely heavily on evolutionary modelling. It remains uncertain whether there are significant shortcomings in the physics of the models, or if the observations are insufficient to explain these stellar objects. In contrast, asteroseismology has been very effective for determining the global properties of the sun and solar-like oscillators (Kjeldsen & Bedding 1995; Bedding 2014).

Two factors significantly contribute to these failures Firstly, rotation rates of single stars are not easily determined and are more challenging to model in single δ Sct stars where equatorial velocities between 100 and 300 $\mathrm{km\,s^{-1}}$ are often observed (Zorec & Royer 2012). Rotation causes splitting of the non-radial modes into equally-spaced multiplets giving a symmetric spread in frequencies dependent on the structure of the star (Aerts et al. 2010). This relationship breaks down as the rotation rate increases, leading to a

★ E-mail: margaret.streamer@anu.edu.au (MS)

complex pattern of pulsation frequencies which are difficult to analyse without the high quality data only now available with space-based probes.

Secondly, the fundamental properties, such as mass and radius and hence density, of any single star are difficult to ascertain with low uncertainties. However, the density of δ Sct stars is a crucial parameter for p mode identification.

Both these short-comings are addressed if a δ Sct star is part of an eclipsing binary system in which all the fundamental properties of both components are open to analysis. Precise models of the stars, with masses and radii determined to 3 % uncertainty, become test-beds for stellar structure and evolutionary models (Torres et al. 2010). If the binary has a short orbital period, the system is almost certainly tidally locked. This gives the rotation period for the pulsating component to an accuracy unavailable for single stars.

Many studies have identified the observed frequencies of δ Sct pulsators (Murphy et al. 2014; Kahraman Aliçavuş et al. 2017; Lee et al. 2019; Yang et al. 2019). However, few have identified specific modes of pulsation; examples include short period binaries such as TT Hor (Streamer et al. 2018) and CoRoT 100866999 (Chen et al. 2019). Others are hybrid pulsators in eccentric orbits, such as KIC 10080943 (Schmid & Aerts 2016) and KIC 4142768, (Guo et al. 2019).

Modelling of δ Sct stars in the instability strip has exposed discrepancies between observed and predicted results. Their masses (1.5 to 2.5 $M_{\odot}$) position them in the transition area of energy transport, having both a tiny convective core and a shallow convective envelope overlying a radiative envelope. Cooler δ Sct stars ($T_{\rm eff}$ ≈7000 K) at the red end of the instability strip have more substantial convective envelopes compared to their counterparts at the blue edge. At the red end, the cooler δ Sct stars overlap with γ Dor stars (Kaye et al. 1999) where γ Dor - δ Sct hybrids are also found (Grigahcène et al. 2010). γ Dor stars exhibit non-radial, g modes, with periods from one to 5 d.

The boundaries of the instability strip are being widened as more δ Sct stars are detected from space-based observations (Bowman & Kurtz 2018; Murphy et al. 2019). These new boundaries lie beyond the theoretical boundaries determined by Dupret et al. (2009). Additionally, Murphy et al. (2019) showed that the fraction of pulsators found at the red edge is less than that at the blue edge, with the fraction peaking at 70% in the middle of the instability strip. Notably, there are normal A-stars showing no pulsations at the micro-magnitude detection limit within this region. The reasons why some stars within the instability strip pulsate and others don't remain largely a mystery (Balona & Dziembowski 2011).

A systematic relationship linking seismic properties to fundamental stellar properties in δ Sct stars has been sought but with limited success. The long-standing association between period, luminosity and colour is often used to identify pulsation modes in these stars (Breger & Bregman 1975). This has been extended recently to include luminosities derived from *Gaia* DR2 parallaxes (Ziaali et al. 2019). García Hernández et al. (2015, 2017) presented a relationship between surface gravity and the large frequency separation of δ Sct pulsations for a small sample of eclipsing binaries with a δ Sct-type component. This was followed by Forteza et al. (2018, 2020) providing an empirical relationship between the frequencies of several hundred δ Sct stars at maximum power and their mean $T_{\rm eff}$.

Significantly, Bedding et al. (2020) detected regular sequences of high-frequency pulsations in a sample of 60 young stars, some from known young stellar associations. The regular sequences allowed the first definitive mode identification for a group of δ Sct stars and is an important identifier of young stars. This paper highlighted the need for well-constrained systems with dynamically-derived masses. As we show in this paper, binary systems are ideal for deriving not only the masses but all the fundamental properties of the δ Sct component.

Different excitation mechanisms further complicate mode identification. The self-excitation of δ Sct pulsations via the κ mechanism remains the most common and operates primarily in the HeII partial ionisation zone. In hotter δ Sct stars, this zone is closer to the surface and more efficient, yielding higher frequencies compared to cooler stars (Pamyatnykh 2000; Bowman et al. 2016; Smalley et al. 2017). Additionally, turbulent pressure in the outer, convective envelope contributes to the driving of pulsations at the red end of the instability strip (Antoci et al. 2014; Aerts 2019; Antoci et al. 2019). In close binary systems, tidal excitation of non-radial modes may also occur and is most evident in eccentric binaries where the frequencies are at exact multiples of the orbital period (eg. Hambleton et al. 2017; Fuller 2017). Oblique pulsators have been confirmed where tidal trapping of modes occurs in close binary systems where the pulsation axis coincides with the line of apsides (Handler et al. 2020; Kurtz et al. 2020).

Evolutionary modelling of stars in the instability strip has also exposed discrepancies between observed and predicted results. For example, the mixing processes, such as convective-core overshooting, are still poorly constrained despite them having a major impact on evolutionary models. For example, Tkachenko et al. (2020) found that discrepancies between binary star observations and models for intermediate- to high-mass stars were overcome by increasing the convective core mass and the mixing near the core. Deal et al. (2020) suggested that current modelling codes, including MESA (Paxton et al. 2011, 2013, 2015, 2018, 2019), lack a process to explain chemical element transport for stars with masses $> 1.4\,{\rm M}_{\odot}$. Their results showed that iron was accumulated at the surface due to radiative acceleration with or without rotation, a result conflicting with *Kepler* Legacy star observations. While not specific to the mass range for δ Sct stars, both studies highlighted the current theoretical difficulties for modelling intermediate mass stars with their conclusions impacting on δ Sct stars in a similar way.

Non-interacting, detached, eclipsing binaries with a δ Sct component are arguably the ideal systems for determining fundamental stellar parameters as the pulsator's properties are most similar to those of isolated stars. However, they generally have orbital periods in excess of 13 d (Liakos & Niarchos 2017) which can limit the number of complete orbital cycles observed. This is particularly relevant for *TESS* observations when only one month's data are available. Ground-based data, subject to short observation times and weather conditions, are also problematic for long-period binaries.

Unlike the latter, Algol-type systems typically have orbital periods < 4 d allowing multiple, full-orbital sequences

to be observed. Algol-types are semi-detached systems with the added dimension of mass transfer occurring during their evolution. Briefly, the initial, higher-mass star evolves the fastest, fills its Roche lobe and then donates mass to its less-evolved component which in turn becomes the higher mass star.

Our line of study concerns δ Sct stars in Algol-type systems with low total-mass of $\approx 3\,M_{\odot}$. The mass transfer is generally conservative, that is, no mass is lost from the system. In our previous paper, (Streamer et al. (2018), referred to as MS18 hereafter), we successfully derived the fundamental parameters of the TT Hor binary system and modelled the binary evolution with the MESA code. Importantly, we refined the evolutionary models, within uncertainties of the binary model, to match and identify the modes of the observed pulsation frequencies. This was achieved because the system was tidally locked and the rotation rate of the δ Sct star was known to high precision from the orbital period.

Streamer et al. (2016) first recognised δ Sct pulsations in the light curve of RZ Mic which was initially categorised as an eclipsing variable star by Hoffmeister (1956). In this paper, we combined data for RZ Mic from *TESS* (Ricker et al. 2015) with our ground-based photometry and spectroscopy to determine the fundamental parameters of the binary system and analysed the observed oscillations after subtraction of the binary light curve. From this basis of a well-characterised pulsating star, including its density and rotation period, we identified the dominant pulsation frequency as a mixed mode.

We conclude that certain binary systems are ideal for identifying modes of δ Sct stars and hence the fundamental parameters of a cohort of single stars with similar frequency patterns and low rotational velocities ($\leq 50\,\mathrm{km\,s^{-1}}$).

2 OBSERVATIONS AND DATA REDUCTION

2.1 Photometry

Data for RZ Mic (TIC 91369561) from *TESS* were taken from 2018, July 25, over 28 days with a 2-min cadence with Sector 1, camera 1. The light curve data were downloaded after systematics removal (cotrending) performed by the SPOC algorithms.

Time-series photometry was also performed with a 0.35 m Meade Schmidt-Cassegrain telescope situated in Murrumbateman, NSW, Australia, IAU observatory code E07. The telescope was equipped with an SBIG ST8XME camera with Johnson B and V filters, and a Cousins I filter.

We synchronized the computer's clock to UTC using the Network Time Protocol.[1] A fast cadence ensured good coverage of the pulsations and accurate determination of the eclipse times of minima. Typical exposure times were 60 to 120 s with delays between each exposure (for image download and filter change) of about 30 s. RZ Mic was observed during secondary eclipses and out of eclipse for as long as possible in any one night to maximise the time span available for Fourier analysis of the pulsations. We made observations in 2014 and 2015 which are available on the AAVSO website[2].

RZ Mic (RA: 20 50 16.387, Dec: -42 13 04.598) is in a sparse field and scrutiny of a high resolution image from the Digitized Sky Survey catalogue [3], 2MASS (Skrutskie et al. 2006) and *TESS* showed no background contaminating stars to affect the photometry.

GSC 7972 0135 was used as the comparison star: V = 11.251 ± 0.041 mag, B−V = 0.53 mag. GSC 7972 0230 was used as a check star: V = 13.005, B−V = 0.49 mag, to assess background changes. Magnitudes are taken from the AAVSO Photometric All-Sky Survey (APASS). The APASS i' magnitude data were converted to Cousins I filter magnitudes using Eqn.1

$$V - I_c = 0.37450 + 1.09888(V - i') \quad (1)$$

The data were reduced with aperture photometry using MaxIm DL [4] and transformed using standard stars from Landolt fields (Landolt 2007). RZ Mic is outside the Galactic plane at a latitude of −39°. We corrected our data for interstellar reddening according to Schlafly & Finkbeiner (2011)

To enhance this data, observations in the B band only were collected in 2019 August 05-31, using the Las Cumbres Observatory (LCOGT) 0.4-m telescopes in Australia, South Africa and Chile. However, the final data were intermittent and of too poor quality to be useful.

2.2 Spectroscopy

We obtained spectra using the ANU 2.3-m telescope at Siding Spring Observatory and the Wide-Field Spectrograph, WiFeS (Dopita et al. 2007, 2010). Observations were taken over 3 nights in 2016 mid-October, and again over 3 nights in 2017 early-May. RZ Mic has an orbital period of 3.98 days and at the time of observations we were limited to phases near 0.25, 0.75 and the primary eclipse (phase = 0.0 /1.0) Cloud cover prevented any secondary eclipse observations. Spectra were obtained using the RT560 beam splitter and the B7000 and R7000 gratings for radial velocity (RV) determination. Spectra for spectral classification were taken using the RT560/B3000 combination. The spectra were reduced with pyWiFeS, the data reduction pipeline specific for the WiFeS spectrograph (Childress et al. 2014). To reduce the effect of pulsations on the RVs, blocks of 4 consecutive RZ Mic spectra were taken and alternated with Ne-Ar arc spectra and subsequently co-added in the pipeline. The RVs were thus sampled every 15 to 20 min.

Spectra were dominated by the primary star at all orbital phases, including primary eclipse, with the main absorption features being the Balmer series. The orbit of RZ Mic is inclined to 79° (see Section 3) thus it is not possible to isolate the spectral features of both components even during eclipse minima. There was no evidence of Hα or other emission lines in these spectra.

The temperature of the system was determined from a

[1] DIMENSION 4 (Thinking Man Software, 1992–2014, http://www.thinkman.com/dimension4/)

[2] AAVSO: https://www.aavso.org/

[3] Digitized Sky Survey: https://archive.stsci.edu/cgi-bin/dss_form/

[4] MaxIm DL: https://diffractionlimited.com/product/maxim-dl/

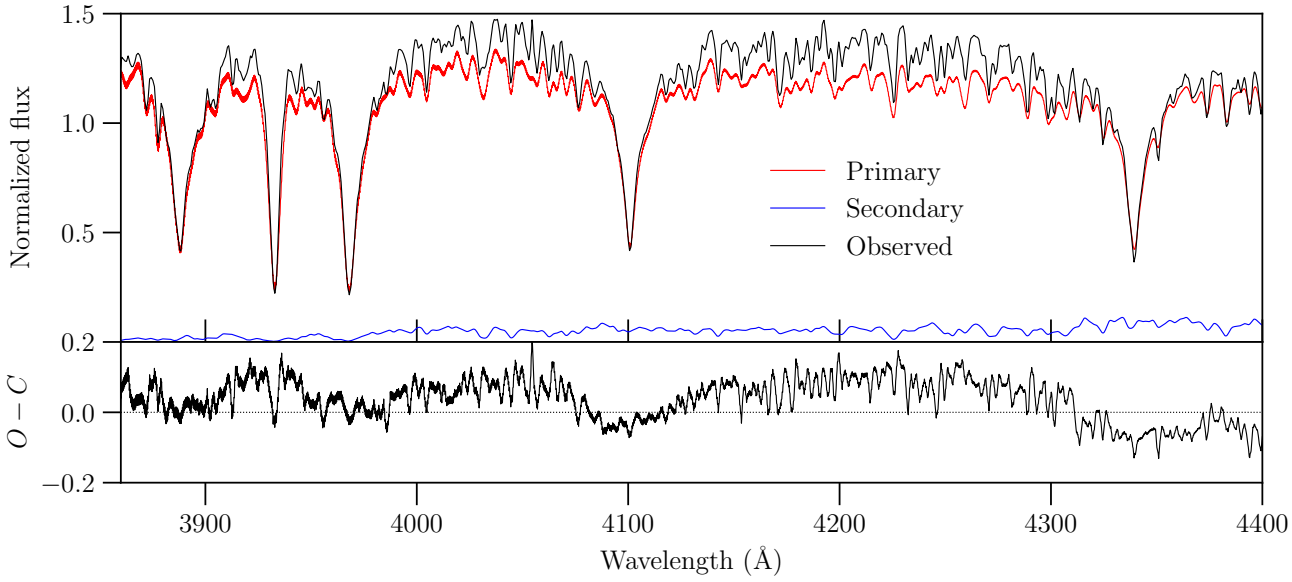

Figure 1. The fit in the Balmer region for the two components resolved by TODCOR.

B3000 spectrum taken at phase 0.5 when there is minimal input from the secondary star. The Spectrophotometric Flux Fitting Method described by Norris et al. (2013) was used[5]. The best fits to the spectrum were $T_{\rm eff}$ =7300 K, $\log g = 4.0$, rms = 0.0336 and $T_{\rm eff}$ =7200 K, $\log g$ = 3.75, rms = 0.0423.

Using the same B3000 spectrum as above, we also resolved the spectra of the two stars with a custom Python interpretation of the two-dimensional correlation function, TODCOR (Zucker & Mazeh 1994). The code uses template spectra to match the spectra of the two components of the binary. Fluxed templates were generated from the synthetic spectra from ATLAS 9 (Castelli & Kurucz 2004) as described in MS18 and a grid-based search was used to determine α, the contrast ratio of the two template spectra. Maximum correlation was found using $\alpha = 0.1$. We used fluxed templates with solar metallicity and $T_{\rm eff}$, $\log g$, $v \sin i$ = [7250 K, 4.0, 50 km s^{-1}] for the primary star and [4250 K, 3.0, 50 km s^{-1}] for the secondary star. Fig. 1 shows the fit in the Balmer region for the separated components compared to the observed spectrum. The primary star fits the hotter template within a flux uncertainty of ± 0.2. There is only a minor flux contribution from the secondary star.

Based on the results from these two methods we assign the $T_{\rm eff}$ of the primary star as 7300^{+200}_{-100} K, corresponding to a A9/F0 star.

RVs of both components were extracted from the B7000 data using normalised templates with solar metallicity and $T_{\rm eff}$, $\log g$, $v \sin i$ = [8000 K, 4.0, 50 km s^{-1}] for the primary star and [4500 K, 3.0, 50 km s^{-1}] for the secondary star, $\alpha = 0.1$. Table 1 gives a list of these RVs. These normalised templates, with an 8000 K template rather than a 7250 K template (as for the fluxed spectra) gave the highest correlation.

Given the domination by the Balmer features, RV measurements for the primary star are more reliable than for the secondary. Uncertainties at quadrature phases (0.25 and 0.75) are lowest, as the components are at maximum velocity and Balmer lines are shifted the most. Shot-noise limited RV uncertainties at these phases for the primary and secondary components are no more than 1 km s^{-1} and 4 km s^{-1}, respectively. Standards stars analysed via TODCOR gave RV uncertainties less than 4.0 km s^{-1}. To create the initial binary orbital model, we therefore used uncertainties of 4 km s^{-1}.

Table 1. Radial velocities determined from TODCOR. RV1 and RV2 are radial velocities for the primary and secondary stars, respectively

Calendar Date	Date HJD	Orbital phase	RV1 km s^{-1}	RV2 km s^{-1}
20161016	2457677.90127	0.69	-42.1	-210.4
	2457677.97118	0.71	-25.4	-197.0
	2457677.99453	0.71	-26.7	-205.9
	2457678.00585	0.71	-28.8	-205.0
	2457678.02775	0.72	-25.1	-205.2
20161017	2457678.95626	0.95	-45.9	-68.3
	2457678.97724	0.96	-46.7	-65.7
	2457679.00009	0.96	-44.4	-68.1
	2457679.02324	0.97	-54.5	-74.5
20161018	2457679.95730	0.20	-97.4	84.3
	2457679.99049	0.21	-94.2	88.6
	2457680.01346	0.22	-97.7	76.8
	2457680.04520	0.23	-95.9	90.8
20170508	2457882.26611	0.99	-56.3	-52.3
20170509	2457883.22765	0.24	-95.6	95.2
	2457883.23535	0.24	-94.3	88.3
	2457883.25376	0.24	-95.0	86.1
	2457883.27694	0.25	-96.9	86.8
20170511	2457885.27635	0.75	-26.1	-205.7
	2457885.290631	0.76	-19.2	-199.3

[5] We thank Professor Mike Bessell at ANU for this analysis.

3 BINARY ORBITAL MODEL

For readers unfamiliar with modelling binary systems, we give a short overview of the data and methodology needed. For an in-depth coverage we refer the reader to Prša (2018). To obtain precise parameters for a binary system, photometry and RV data from spectroscopy, covering all orbital phases are ideal. The temperatures of the component stars from spectroscopy are also desirable.

For RZ Mic, we had *TESS* data spanning multiple full orbits, but by themselves these data were not adequate for the model precision we desired. However, the colour indices given by our ground-based photometry in three different passbands (B, V and I) were maintained in our modelling procedure (see subsection 3.1 for more details) providing luminosity constraints to the *TESS* data. The inclination of an eclipsing system and the radii of both components are given by the shape of the light curves in units of the semi-major axis. The relative depths of the eclipses and the colour changes give the surface temperature ratio. We determined the temperature of the primary star (see subsection 2.2) and estimated that of the secondary star from modelling. The luminosity of each star was determined by the following equation.

$$\frac{L}{L\odot} = R^2(\frac{T}{T\odot})^4 \quad (2)$$

where R is the radius in solar units, $T_\odot$ is the solar temperature and T is $T_{\rm eff}$. RVs from spectroscopic measurements give the mass ratio of the stars and, with the inclination, the individual masses of both stars are determined. No additional inputs are required. A more detailed description of the methodology follows.

3.1 Binary Modelling Procedure

Light curves for RZ Mic, including the complete *TESS* data (18,100 data points, covering 7 complete orbits) and V, B and I data from 2014 to 2015 are shown in Fig. 2. The detector bandpass for *TESS* covers a broad region from 6000 to 10000 Å, centred on the Cousins I-band with the mean at 7972 Å. RZ Mic is brightest in the *TESS* passband and dimmest in blue with B−V = 0.39 during uneclipsed phases. The light curves are typical of a semi-detached binary system. The ingress to and egress from the primary eclipse were deeper compared to those of the secondary eclipse, an effect most evident in the *TESS* and I data. The secondary eclipse is also deeper in these data. These effects are indicative of a cool secondary star having filled its Roche lobe.

We used the modelling package, PHOEBE 2.1.4 (Prša et al. 2016; Horvat et al. 2018) to determine a binary model fit to both the photometric and RV data. One of the advantages of this PHOEBE code is the implementation of a triangulated mesh grid to discretise the stellar surface as opposed to the use of trapezoids in the original Wilson and Devinney code (Wilson & Devinney 1971). Among other things, more accurate modelling of non-spherical systems such as those distorted by any Roche-lobe filling star is achieved. A second advantage of this code is that for RZ Mic, and other close binaries where surface irradiation is important, the reflected and intrinsic light are calculated independently.

We performed a preliminary fit to the data using the semi-detached constraint in PHOEBE, setting the secondary star to fill its Roche lobe and fixing the $T_{\rm eff}$ for the primary star to 7300 K. To reduce modelling time for the preliminary fit, *TESS* data were binned every 20 data points according to orbital phase. From the RV data, we estimated the mass ratio and system velocity. An initial, approximate fit by eye was done using a coarse mesh grid and turning irradiation off. We varied the system inclination, radius and mass of the primary star, and temperature of the secondary. We used blackbody atmosphere models with logarithmic limb darkening as the temperature gradient across the secondary star was too great for CK2004 atmosphere model tables to be effective (Castelli & Kurucz 2004). The gravity darkening coefficients for the primary and secondary star were fixed at 1.0 and 0.32, respectively, for a radiative star or a convective star (Lucy 1967).

Using this preliminary model as a guide and a coarse grid mesh, we set best guesses for the parameters to be fitted in an EMCEE routine (Foreman-Mackey et al. 2013). These were: orbital inclination; equivalent radius of the primary star; irradiation fraction of the primary; $T_{\rm eff}$ of the secondary star; mass ratio (q); semi-major axis of the system; and the system velocity. Furthermore, we constrained $T_{\rm eff}$ = 7300 K for the primary star; used the irradiation method according to Horvat et al. (2019) in which we fixed the reflected irradiation to 1.0 for the primary star and 0.6 for the secondary; a coarse grid mesh and logarithmic limb darkening function with blackbody atmosphere tables.

It was obvious that the photometric residuals in this initial fit were dominated by the pulsations in the primary star. Rather than attempting a highly complex simultaneous fit of the pulsations and the binary, we subtracted this initial model of the binary and modelled the pulsations (as described in Sections 3.2 and Section 4). The modelled frequencies were then subtracted from the initial binary model. This pre-whitening procedure left us with light curves free of pulsations in order to better characterise our binary model. Using this pre-whitened data, we computed the mean square errors (MSE) for each of the 6 data sets (4 light curves and 2 radial velocity curves), and individually scaled their uncertainties to give updated mean square errors of 1.0. When re-examining the plot of the photometric residuals, they were clearly correlated over a data length of approximately 25, especially around the primary eclipse. To account for this non-diagonal covariance matrix in a simple way, we chose to scale the uncertainties by this correlation length. This gave the empirical input uncertainties to our final EMCEE run according to the following equations:

$$\mathrm{Error_{new}} = \mathrm{Error_{orig}}\sqrt{\mathrm{MSE}} \text{ for RV data} \quad (3)$$

$$\mathrm{Error_{new}} = \mathrm{Error_{orig}}\sqrt{\mathrm{MSE}}\sqrt{25} \text{ for photometric data.} \quad (4)$$

By scaling the uncertainties on the input appropriately, the error bars derived from the posterior in EMCEE are much more robust and reliable. The re-scaling of the uncertainties of the RV data gave the adjusted RV uncertainty for the primary as 6 km s^{-1} and for as 13 km s^{-1} for the secondary for each RV point, as shown in Fig. 3. This results in 5 and 2 km/s uncertainties for the fitted semi-amplitudes. We also note here that EMCEE gave us the density of the primary star with uncertainties which are lower than the uncertainties one would obtain by assuming mass and radius are independent. This is because the mass and radius posteriors are

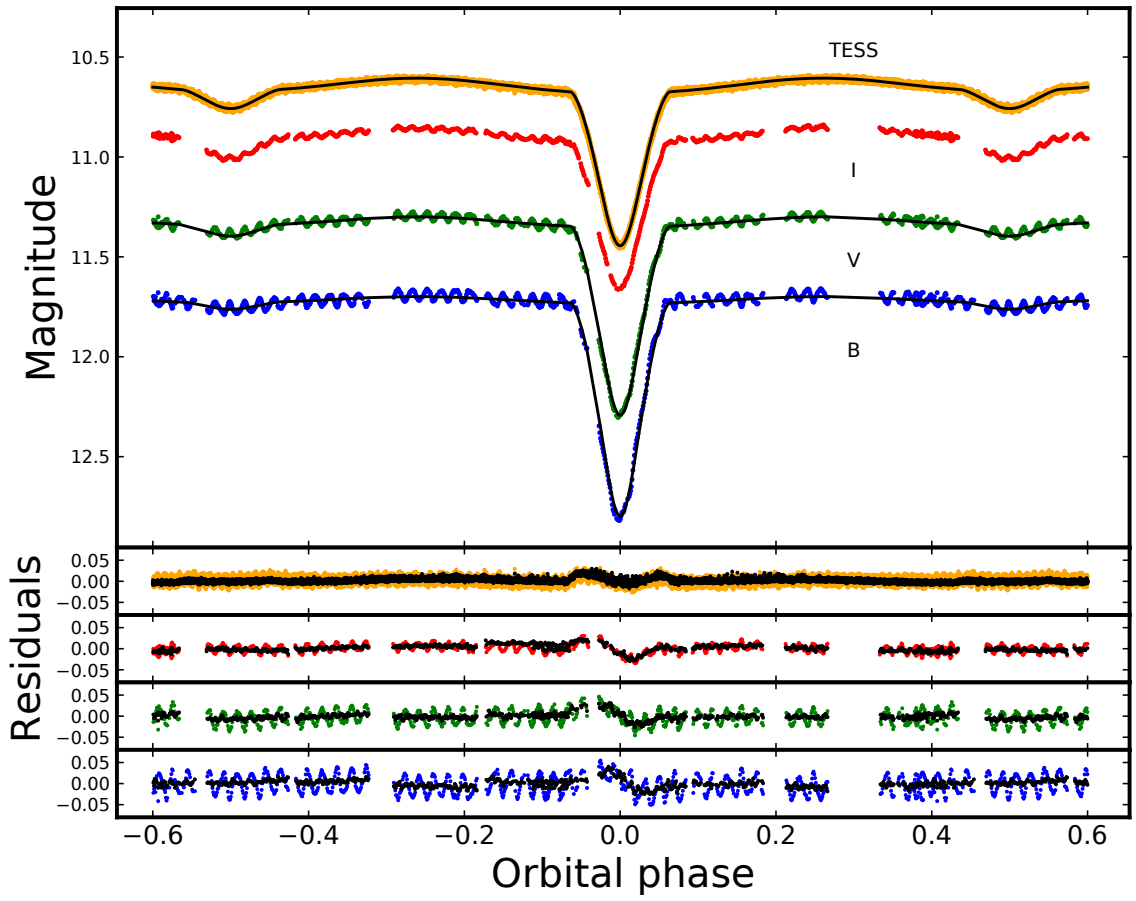

Figure 2. Magnitude changes of RZ Mic with orbital phase using different filters. From top to bottom: orange = *TESS*, Red = I filter, Green = V, Blue = B. The binary models for each filter are indicated by the black solid lines. The residuals after removal of the binary models for each filter are plotted below. The black points on the residuals plots are those given for each filter after subtraction of the pulsations and remodelling the binary system. Firstly, we subtracted the binary model from the original data sets, then extracted the pulsation frequencies from the latter, and finally subtracted these frequencies from the original data. Then we re-modelled the binary with this data and plot the residuals. The standard deviation for the magnitude of the check star was typically 0.005.

highly correlated: both with uncertainties dominated by the radial velocity measurements that define the overall scale of the binary. We calculated the primary star's mass from the orbital period, semi-major axis and q values for every EMCEE realisation of the posterior. Then, combined with its radius, determined the density. The final value of density is $0.213 \pm 0.006\,\mathrm{g\,cm^{-3}}$ which corresponds to a 2.9 % uncertainty. This is an important value which we shall refer to later in Section 6.

The values of each parameter given by EMCEE were then used in the final binary model with PHOEBE using a fine mesh grid of 1500 triangles, Horvat irradiation, and the full *TESS* data set in order to compute the finely gridded residuals and light curves in Fig. 2.

3.2 Binary Model Fit

The model light curves for each passband are indicated in Fig. 2 by the solid black lines over-plotted on the observed data. When fitting and plotting, the filter zero points for the model were left as free parameters. This means that the fit was distance and reddening-independent. The data from each filter are represented in different colours. Pulsations were clearly evident in the V, B and I data but were impossible to differentiate in the *TESS* phased data as several complete orbits were covered. The residuals for each passband reflected the small imperfections of the model-fit around the primary eclipses where pulsations were also evident. Pulsations were not synchronised with the orbital period, thus increasing the spread of residuals around primary eclipse. The black points in the residual plots represent the residuals from the pre-whitened binary model.

The binary model fit to our RV data is shown in Fig. 3. We determined the system velocity as -59.9 ± 1.3 $\mathrm{km\,s^{-1}}$ which compares favourably with the median value given by Gaia DR2 of -56.65 ± 7.57 $\mathrm{km\,s^{-1}}$. We had insufficient spectra covering phases either side of the primary eclipse to investigate the Rossiter-McLaughlin effect (Rossiter 1924). Thus, the alignment of the orbital and spin axes remains unknown.

Table 2 lists the parameters for both stars and the system. The PHOEBE model confirmed the semi-detached nature of RZ Mic, consisting of a $2.18 \pm 0.01\,\mathrm{M_\odot}$ primary (here-

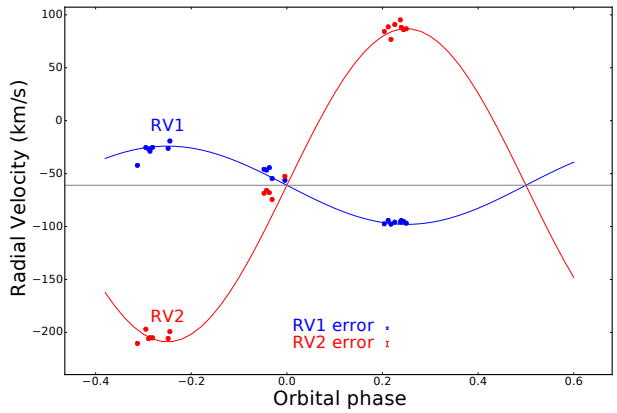

Figure 3. RV variations of the primary (blue dots) and secondary (red dots) stars with the orbital phase of the binary system. The solid lines are the binary model fit. The error bars indicate the uncertainties at quadrature phases.

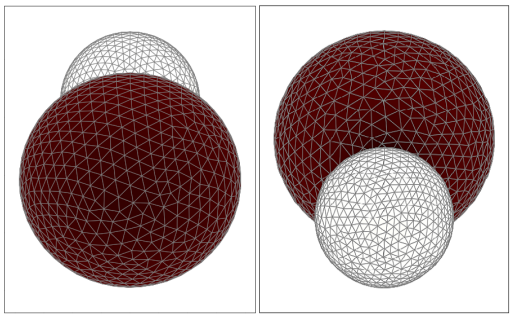

(a) primary eclipse (b) secondary eclipse

Figure 4. Relationship of the primary, δ Sct star (white) and the secondary star (brown) at primary and secondary eclipses

after termed the accretor) and a $0.57 \pm 0.02\,M_\odot$ secondary (hereafter termed the donor). As stated previously, we fixed $T_{\rm eff} = 7300$ K (refer to Subsection 2.2) for the accretor for the modelling which gave $T_{\rm eff} = 4373$ K for the donor which was consistent with that from our TODCOR analysis. The ± 25 K error for the donor is a statistical error only for the fixed temperature of the accretor. We therefore assigned $T_{\rm eff} = 4373 \pm 100$ K for the donor (taking into account the effect of the primary star temperature uncertainty). From the model temperatures and luminosities, the donor was likely an H-shell burning, K5-giant.

Fig. 4 shows the scaled relationship between the two components at phases 0.25 and 0.75. The orbital axis was inclined to our line-of-sight, so each eclipse was partial. The secondary star was estimated to contribute 13% to the B-band flux, 22% to the V-band flux and 34% with the *TESS* filter at secondary eclipse (refer to subsection 3.3 for further details).

The temperature and log g profiles across the surface of the two stars are shown in Fig. 5 and Fig. 6. Note in these plots that the relative sizes of the two components are not to scale but they are in their correct orientation. The secondary star varied in $T_{\rm eff}$ from just below 4500 K to its coolest of ≈ 3800 K at the 'nose'. The primary star was hottest at the poles, and coolest at the face away from the secondary star but the temperature difference was only ≈ 25 K. The log g profile of the secondary star was fairly uniform, ≈ 3.0 except at the 'nose' where it declined to about 1.8. Similarly the log g profile of the primary star was lowest on the face towards the secondary star, but otherwise fairly uniform.

The binary model was consistent with RZ Mic being an Algol-type binary where the donor had evolved to fill its Roche lobe with a radius of $3.973\,R_\odot$. The temperature and log g variations in both stars were consistent with mass loss from the secondary star at the 'nose' and this mass impacting the primary star on the face closest to the donor star. We observed the system when the accretor was the more massive star having gained considerable mass from the donor.

3.3 Luminosity

We estimated $\log(L/L_\odot)$ for the accretor from its radius determined by binary model and it's $T_{\rm eff}$ from our spectroscopy. Similarly, we calculated $\log(L/L_\odot)$ for the donor using both its radius and $T_{\rm eff}$ from the binary model (Table 2). We compared this to the Gaia DR2 published result of $\log(L/L_\odot) = 1.33$ for the system, which used the methodology described by Andrae et al. (2018). We then used the latter method to determine the luminosity uncertainties from the distance uncertainties from Gaia parallax measurements using Eqn. 5, where M_G is the absolute g-band magnitude, G is the mean magnitude of 11.246 ± 0.002, A_G is the extinction in g band and r is the Gaia DR2 distance in pc.

$$M_G = G - 5\log_{10} r - A_G \tag{5}$$

The luminosity (L_b) for the system was then calculated using the standard equation (Eqn. 6), where $BC_G = 0.06$ is the bolometric correction for $T_{\rm eff}$ of 7300 K and the bolometric magnitude of the sun, $M_{\rm bol\odot} = 4.74$.

$$-2.5\log_{10} L_b = M_G + BC_G(T_{\rm eff}) - M_{\rm bol\odot} \tag{6}$$

The total luminosity of the system was thus calculated as $\log(L/L_\odot) = 1.33 \pm 0.05$.

We used the `blackbody_lambda` function from `astropy.modeling.blackbody` (Robitaille et al. 2013; Collaboration et al. 2018) to estimate the proportion of flux due to the secondary star at the midpoint of the Gaia g-band 6730Å. This amounted to 34% of the total flux giving the luminosity for the accretor alone as $\log(L/L_\odot) = 1.15 \pm 0.05$. Our $\log(L/L_\odot) = 1.18 \pm 0.03$ for the accretor from the binary model was well within the uncertainties from the Gaia determination. This gave us additional confidence in the radius of the accretor determined from our binary modelling and its $T_{\rm eff}$. Table 2 also tabulates the absolute Gaia DR2 magnitudes of the primary, secondary and system and the bolometric corrections used from Andrae et al. (2018).

Table 2. The parameters of RZ Mic as determined by PHOEBE from combined photometry and spectroscopy. The Gaia Log(L/L$_\odot$), the relevant bolometric correction for each star at their given temperatures (BC$_G$($T_{\rm eff}$)) and absolute magnitudes (M$_G$) are given here for comparison. The reader is referred to subsection 3.3 for a discussion of Gaia values.

Parameter	Primary (accretor)	Secondary (donor)	System
Orbital period (days)	-	-	3.98305 ± 0.00001
Semi-major axis (R$_\odot$)	-	-	14.79 ± 0.22
System velocity (km s^{-1})	-	-	-59.9 ± 1.3
Semi-amplitudes, K (km s^{-1})	37 ± 2	145 ± 5	
Inclination, (°)	-	-	79.45 ± 0.14
M_2/M_1 (q)	-	-	0.256 ± 0.006
M (M$_\odot$)	2.18 ± 0.10	0.57 ± 0.02	
R (R$_\odot$)	2.43 ± 0.05	3.973 (fixed)	
$T_{\rm eff}$ (K)	7300^{+200}_{-100}	4373 ± 25[a]	
log g	4.0 ± 0.01	2.6 - 3.0	
Log(L/L$_\odot$)	1.18 ± 0.03	0.72 ± 0.03	
Gaia Log(L/L$_\odot$)	1.15 ± 0.05	0.86 ± 0.05	1.33 ± 0.05
BC$_G$($T_{\rm eff}$)	0.06	-0.02	0.06
M$_G$	1.67 ± 0.12	2.39 ± 0.12	1.22 ± 0.12

[a] As EMCEE used a fixed primary temperature, this temperature uncertainty for the secondary star should be viewed as an uncertainty in the temperature ratio between primary and secondary stars as constrained by the wavelength-dependent eclipse depths. An additional ~100 K uncertainty would arise from the uncertainty from primary temperature.

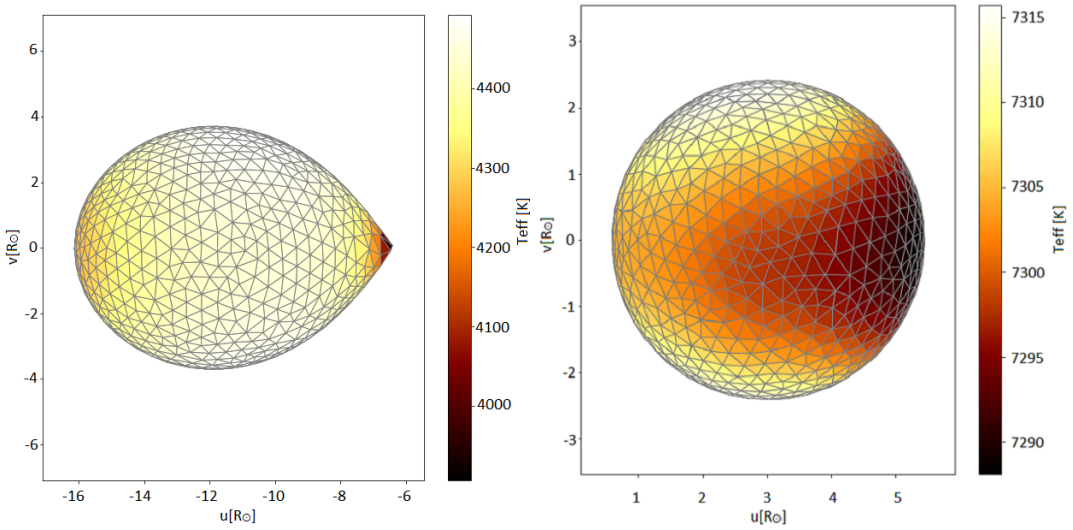

(a) secondary star (b) primary star

Figure 5. Temperature profile of primary and secondary star with respect to the observer on the uv plane-of-sky coordinates.

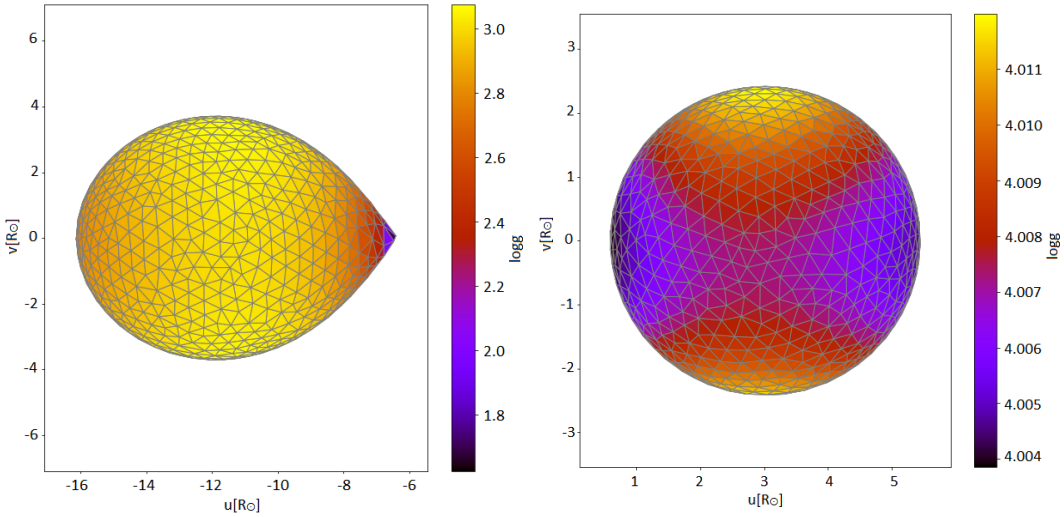

(a) secondary star

(b) primary star

Figure 6. $\log g$ profile of primary and secondary star with respect to the observer on the uv plane-of-sky coordinates.

We also independently estimated the distance to RZ Mic using the V magnitude (11.56) at secondary eclipse and the luminosity of the accretor from the binary model. This gave a distance of 916 pc, compared to the Gaia DR2 of 959 ± 56 pc. Thus our calculated distance is within the uncertainties of the Gaia estimation.

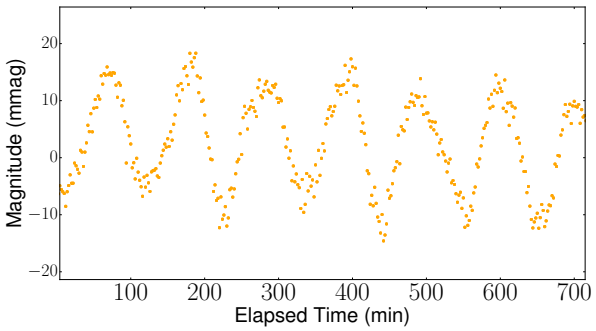

Figure 7. An example of the *TESS* residuals after subtraction of the binary model.

4 PULSATION ANALYSIS

The *TESS* data have the continuity and time span ideal for Fourier analysis of the oscillations. The binary model for RZ Mic was subtracted from the *TESS* data and the residuals were used for a Fourier transform using PERIOD04 (Lenz & Breger 2005). An example of the *TESS* residuals covering about 10 h are shown in Fig. 7. Low-power frequencies from 0 to $8\,\mathrm{d}^{-1}$ were not included in the analysis as they were harmonics of the orbital frequency of the binary system and hence, artefacts from the imperfect binary model fit. After calculating the linear least-squares fit, a non-linear least-squares fit improved the true frequency by assessing the amplitude and phase together with the frequency.

The Fourier transform of the frequencies $> 8\,\mathrm{d}^{-1}$ showed one dominant frequency, f_1, at $13.522\,\mathrm{d}^{-1}$ plus two of lower amplitudes at $25.617\,\mathrm{d}^{-1}$ (f_2) and $20.279\,\mathrm{d}^{-1}$ (f_3) (Fig. 8 a). Fig. 8 b shows the frequencies around f_1 after prewhitening of this. One frequency, f_8, was evident at this stage and remained after subsequent prewhitening of f_2 and f_3. Additional low amplitude frequencies of about 0.3 mmag were also evident in multiples of the orbital frequency as labelled in Fig. 8 b as $f_1 \pm \mathrm{n}\ f_{\mathrm{orb}}$. None were exact integer values of the orbital frequency. These frequencies were likely artefacts caused by the imperfect binary model fit, plus a slightly larger scatter of data points in the second half of the *TESS* data compared to the first half.

Fig. 9 a and b show the additional frequencies extracted about f_2 and f_3, respectively, after subsequent prewhitening. f_4 was an independent frequency at $26.681\,\mathrm{d}^{-1}$, as were the much lower-amplitude frequencies of f_6 and f_7. The frequencies, f_5, f_8, f_9 and f_{10} were all related to f_2 as indicated in Table 3. Frequencies were extracted until the S/N was <4, the recommended limit by the authors of PERIOD04. The total of fourteen frequencies are listed in Table 3, together with their relationship, if any, to the orbital frequency.

There was no evidence that the f_1 frequency was a result of rotational splitting of high-frequency modes. The other frequencies were all independent although, as shown in Table 3, four frequencies were close to being exact multiples of the orbital frequency. Apart from f_8, the uncertainties associated with these frequencies were too large for any orbital relationship to be definitive and could simply be coincidental because of incomplete removal of the binary orbit. We could speculate that the relationship was indicative of tidally-excited oscillations (Fuller 2017) with the driving mechanism being a small, undetected eccentricity ($< 0.01\%$) in the system. However, the frequencies were too high to be g-modes as found in typical eccentric binaries (Hambleton et al. 2017).

Pulsations were evident in all ground-based data obtained from Murrumbateman. We analysed data from four consecutive nights with excellent seeing conditions from 2014 August 03 - 06. Only the B and V observations were

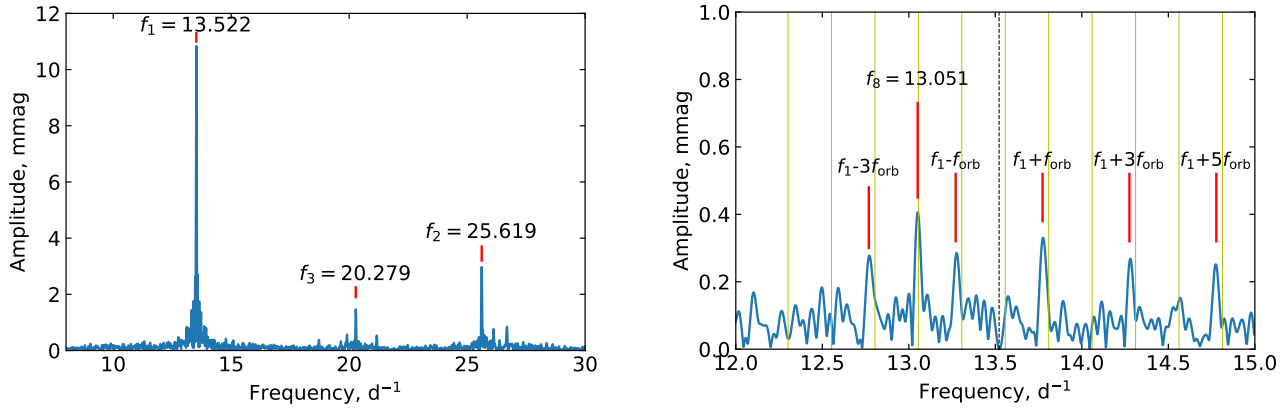

(a) main frequencies

(b) frequencies after prewhitening f_1

Figure 8. Original frequencies extracted (a) and subsequent frequencies after prewhitening of f_1 (b). The red solid lines indicate the extracted frequencies. In (b), the black, vertical, dashed line indicates the position of f_1 and the thin, vertical orange lines indicate multiples of the orbital frequency, 0.251 d^{-1}.

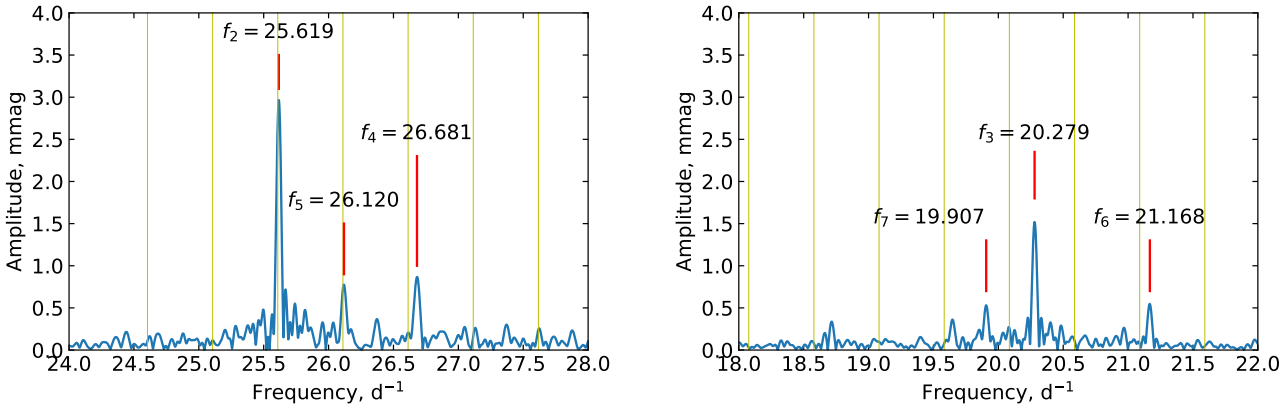

(a) additional frequencies near f_2

(b) additional frequencies near f_3

Figure 9. Frequencies around f_2 and f_3. The vertical lines are as described for Fig. 8.

Table 3. The frequencies with their amplitudes extracted from the *TESS* data. M-C is the uncertainty given by a Monte-Carlo simulation. Freq$_n$/f_{orb} indicate the number of f_{orb} (= 0.251 d^{-1}) in the identified frequency.

	Freqency d^{-1}	M-C d^{-1}	Freq$_n$/f_{orb}	Amplitude mmag	S/N
f_1	13.522	0.001		10.863	16.81
f_2	25.619	0.071	102.040	2.846	23.40
f_3	20.279	0.001		1.513	14.26
f_4	26.681	0.002		0.828	6.63
f_5	26.120	1.187	104.036	0.707	6.12
f_6	21.168	7.623		0.552	8.13
f_7	19.907	0.002		0.493	6.29
f_8	13.051	0.003	51.984	0.403	4.39
f_9	25.592	0.421	1.001	0.536	6.15
f_{10}	26.373	1.204	105.045	0.341	3.39
f_{11}	18.716	1.533		0.339	5.32
f_{13}	13.777	0.005		0.340	3.93
f_{14}	19.645	0.005		0.316	4.36

analysed with PERIOD04 as pulsations in the I band were too low for confident analysis. The orbital effects were first removed by fitting a simple, low-degree polynomial function to the short data sets, none of which included either of the eclipse phases. These data gave similar frequencies as the *TESS* data for f_1 and f_2 (Table 4). Additionally, two other frequencies, (either 21.19 d^{-1} or 19.65 d^{-1}) were found in the B and V data. The former is probably equivalent to f_6 and the latter to f_3 identified in the *TESS* data, with both having much lower amplitudes of 1 to 2 mmag in the B and V data. Compared to the *TESS* results, the f_1 pulsations in the B and V data were of considerably higher magnitude (145% and 74%, respectively). In contrast, for f_2, the difference in amplitude was only 77% and 34% in the B and V data. An intensity change is expected with different filters, with the blue filter having the largest, because of the black body curves. Additionally, the pulsation amplitude at different wavelengths is affected by the relative temperature changes and the cross-section changes of the star (Aerts et al. 2010; Garrido et al. 1990). Such effects can constrain mode

identification but as yet there is no generalised method for doing so. All we could conclude was that our data may indicate that there was a strong depth effect in the atmosphere for f_1 which was far less for f_2.

5 EVOLUTIONARY MODELLING

Evolutionary modelling of any binary system in which mass is transferred from one star to its companion requires a considerable number of free parameters. Mass transfer can be either conservative, with no mass loss from the system, or non-conservative where mass is lost from the system. In the latter case, the initial, total pre-main-sequence mass of the system and the amount of mass lost from the system are unknown and are therefore additional free parameters in the evolutionary controls governing each star. With conservative mass transfer, the task is somewhat easier as the initial and final masses of the system are the same, so the modelled parameter space is smaller.

5.1 Evolutionary models of binary system

We modelled the RZ Mic system using the Modules for Experiments in Stellar Astrophysics (MESA) software suite, version -r11701. We performed a grid search by fixing the total mass of the system equal to that from our binary model to four significant figures (2.742 $M_\odot$) and varying the initial masses for the donor from 1.4 to 1.8 $M_\odot$ and for the accretor from 1.342 to 0.942 $M_\odot$. The initial orbital period was varied from 2.8 to 3.3 d. We considered three values of the convective efficiency parameter, or mixing length, $\alpha_{\rm MLT}$, either 1.6, 1.8 or 2.

The evolution of low-mass binaries (total mass $\leq 3\,M_\odot$) has been successfully modelled with a fully-conservative mechanism for mass transfer (Kolb & Ritter 1990). As with the TT Hor system (MS18), the binary modelling gave no suggestion of an accretion disc or hot spot on the accretor that could drive an outflow of mass from the system. We therefore used the 'Kolb' formalism for conservative mass transfer in MESA.

Using this mass-transfer scheme, and the initial masses and periods as described above, many models terminated because the accretor had expanded in radius to the point of overflowing its Roche lobe before any significant mass gain from the donor. This happens when the donor is at the Hertzsprung Gap. At this point the accretor is unable to increase its mass and remains at about 0.01 $M_\odot$ above its initial mass and therefore unable to evolve into an A- or F-star with the set conditions. Additionally, no suitable models were found with the initial period > 3 d. Little mass had been transferred but the accretor remained well inside its Roche lobe. In these cases, the donor had reached constant luminosity, leading to a long-lived phase of evolution most likely leading to a helium white dwarf precursor as described by Chen et al. (2017).

The only models that successfully evolved to match the dynamical masses all had an initial period of 3.0 d. The initial masses ranged from 1.4 to 1.6 $M_\odot$ for the donor and between 1.342 to 1.142 $M_\odot$ for the accretor. We were able to match the system orbital periods, and the accretor mass to those of the binary model, but the temperatures of the accretor were between 8400 and 9400 K with radii from 2 to 2.18 $R_\odot$, all of which were outside the uncertainties for temperature and radius for the accretor ($T_{\rm eff} = 7300^{+200}_{-100}$ and radius $= 2.42 \pm 0.07\,R_\odot$.

Nevertheless, we know from our binary evolutionary models with initial period = 3 d that the time-scale for tidal-locking was $< 200{,}000$ yr, that is, by the time the system reached the ZAMS and long before any Roche lobe overflow began at ≈ 2.4 Gyr. This is typical of close binaries such as RZ Mic, where orbits circularise and co-rotation is achieved on time-scales much shorter than the evolution of the binary. Additionally, co-rotation with the orbit is maintained during conservative mass-transfer (Hurley et al. 2002). Therefore, we know the rotation rate of the accretor to the same certainty as the orbital period of the system.

5.2 Evolutionary models of single stars

As our main goal was to identify the pulsation modes of the accretor, and a considerable number of free parameters was already used for evolutionary modelling of RZ Mic, we chose to simplify the modelling procedure. To this end, we modelled the evolution of the accretor in isolation, as was successful for TT Hor (MS18). This required a reduction in $T_{\rm eff}$ and an increase in the radius of the accretor in our evolutionary models. To investigate stellar models, we generated MIST models (MESA Isochrones & Stellar Tracks) (Dotter 2016; Choi et al. 2016) using the associated web interpolator, for masses from 2 to 2.3 $M_\odot$ with solar metallicity. None of these models matched the log $T_{\rm eff}$ vs log($L/L_\odot$) or the log $R_\odot$ vs log($L/L_\odot$) parameter spaces of the RZ Mic accretor (Fig.10). For clarity, only the MIST models for 2.2 and 2.0 $M_\odot$ are shown. Since no literature values for [Fe/H] for RZ Mic were available, we experimented with increasing this parameter to reduce $T_{\rm eff}$. For [Fe/H] = 0.45 dex, and 2.0 $M_\odot$, we lowered the luminosity sufficiently to give a close match to the accretor (labelled as MIST 2.0, 0.45 in Fig.10). A 2.2$M_\odot$ model with a similar [Fe/H] was not a match, and is not shown in this Figure.

The 2 $M_\odot$ with [Fe/H] = 0.45 dex was just outside the lower uncertainty of the accretor dynamical mass (2.08 $M_\odot$). To refine this MIST model we returned to MESA-r11701. The mass of the single star was set to 2.0 $M_\odot$ and the metallicity adjusted from protosolar values, Z = 0.0134, Y = 0.2704 and X = 0.7381 (Asplund et al. 2009), to Z = 0.03883, Y = 0.3073 and X = 0.6539. This Z value is equivalent to [Fe/H] of 0.476 dex. This metal-enhanced model (MESA 2.0 0.476) is also shown in Fig.10.

For these computations we used photosphere tables from the PHOENIX model atmospheres (Hauschildt et al. 1999a,b), $\alpha_{\rm MLT} = 1.82$ pressure scale heights (H_p) in the Henyey implementation of the mixing length formalism (Henyey et al. 1965) and the Ledoux criterion for convection (Ledoux 1947). Our overshoot values differed from those of MIST, and were: overshoot $\alpha = 0.1$, overshoot (f) above the hydrogen-burning core = 0.01 H_p and $f0$ = 0.008 H_p. The pressure scale height (H_p) for overshooting is limited to the radial thickness of the convection zone divided by overshoot α. $f0$ is a non-zero value for the edge of the convective zone in terms of H_p and f is the H_p of overshoot above the convective zone. Similarly, overshoot, f, below the hydrogen-burning shell = 0.01 and $f0$ =0.008. The full in-

Table 4. Comparison of the frequencies and amplitudes extracted from the *TESS* data and ground-based data

Bandpass	f_1 (d^{-1})	Amp (mmag)	% increase	f_2 (d^{-1})	Amp (mmag)	% increase
TESS	13.522	10.86	-	25.619	2.85	-
B	13.518	26.67	145	25.597	5.05	77
V	13.521	18.93	74	25.589	3.82	34
B-*TESS*		15.80			2.20	
V-*TESS*		8.07			0.97	

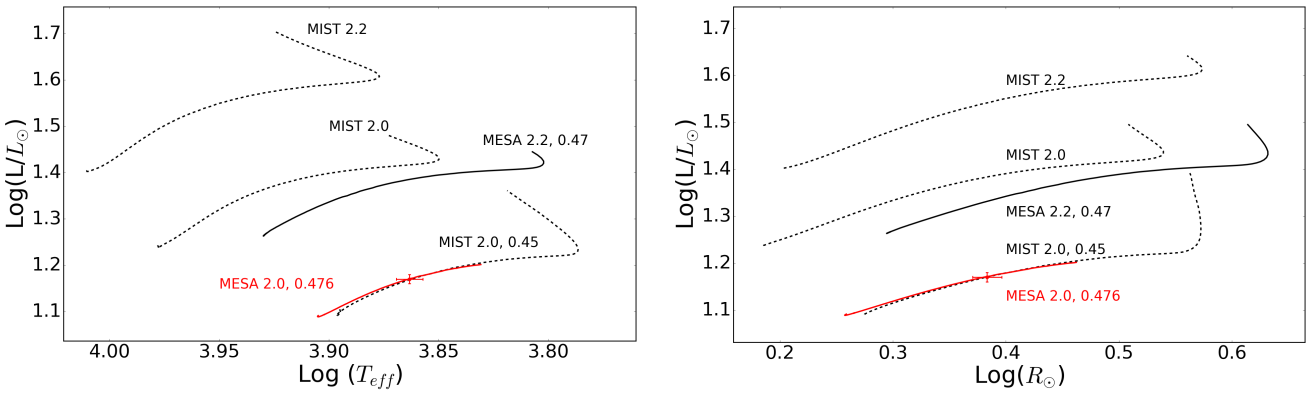

(a) HR diagram, log T

(b) HR diagram, log R

Figure 10. Comparison of MIST and MESA models for single stars matching binary accretor parameters on the main sequence. MIST models are dashed lines and MESA models are solid lines. MIST 2.2 and MIST 2.0 are for masses 2.2 and 2.0 $M_\odot$ with solar values for [Fe/H] and MIST 2.0, 0.45 is for 2.0 $M_\odot$ with [Fe/H] values of 0.45 dex. MESA 2.0, 0.0476 and MESA 2.2, 0.47, are for masses of 2.0 and 2.2 $M_\odot$, with [Fe/H] of 0.476 and 0.45 dex, respectively. The equivalent parameters, plus error bars, for the RZ Mic accretor from the binary modelling are shown in red.

lists were uploaded to the MESA repository which includes the different overshoot values compared to those used in the MIST models.

Again, we used a lower mass compared to the dynamically-derived mass and a high-metallicty to match a single star to the accretor parameters. This suggested that our current evolutionary modelling was insufficient to explain this system. Although we were able to find a satisfactory model for the accretor in the TT Hor binary system (MS18), this also was only achieved after increasing the metallicity. The accretors in both systems have similar masses (2.22 $M_\odot$) but TT Hor has a higher $T_{\rm eff}$ (8800 K) and smaller radius. In other words, MESA was computing similar models for both systems but a higher metallicity correction was needed for RZ Mic as it has a lower temperature.

A-type stars are particularly difficult to model because of their intermediate mass, where they transition from a predominantly radiative core and deep convective envelopes, as for low-mass stars, to a convective core and radiative envelopes, as for high-mass stars. The convective core in late A- to early F- stars is very small with the radiative layer being surrounded by a thin convective envelope which extends to high optical depth. Increased metallicity increases the opacity beneath the convective zone directly. Increased opacity then increases the radiation pressure in the envelope driving expansion, resulting in larger radii and lower $T_{\rm eff}$ (Iglesias & Rogers 1996).

Metallicity also has a crucial role in determining the appropriate mixing length parameter for understanding the stellar structure. Several authors have looked at the degeneracy between $\alpha_{\rm MLT}$ and metallicity in the giant branch (Tayar et al. 2017; Li et al. 2018) and in metal-poor stars (Joyce & Chaboyer 2018). If the bulk abundance is wrong, the stellar radius and effective temperature are not likely to be correct and therefore, the observations are not matched. 3D, hydrodynamic model atmospheres of convection in cool stars are probably needed to explain the role of metallicity on these types of stars as indicated for red giants by Li et al. (2018). However, models for A/F stars were not included in the Stagger grid (Magic et al. 2013) because the near-surface structure of these stars is very different in 3D compared to 1D and atomic diffusion and gravitational settling is difficult to model.

Until there is improvement in theoretical models, successful evolutionary modelling of single stars in the transition zone of the instability strip will remain particularly difficult. Our minimal solution to match our dynamically-derived parameters for the accretor was achieved by increasing its opacity via increasing metallicty.

6 MODE IDENTIFICATION

Despite the limitations to our single-star models (Subsection 5.2), we proceeded to investigate the modes of our observed frequencies. We reiterate that any model may not be realistic given the difficulty of finding an appropriate mixing length parameter and the high metallicity required to match

Table 5. Comparison of the accretor parameters from binary modelling (Accretor) and single star evolutionary model (Model) used for mode identification. The uncertainties for the accretor parameters from binary modelling are listed as 'Error'.

	Mass $M_\odot$	Radius $R_\odot$	$T_{\rm eff}$ (K)	Luminosity Log($L/L_\odot$)	Density g /cm^3
Accretor	2.18	2.43	7300	1.18	0.213
Error	0.10	0.05	200	0.03	0.006
Model	2.00	2.34	7363	1.16	0.219

Table 6. Identification of the observed frequencies from the *TESS* data.

	Observed (d^{-1})	Identified (d^{-1})	difference %	Mode ID n,l,m
f_1	13.522	13.584	0.46	1,1,-1
f_2	25.619	25.592	0.11	4,2,-2
f_3	20.279	20.262	0.08	3,1,1

the accretor parameters. We investigated four single-star masses (1.98, 2.0, 2.02, 2.04 $M_\odot$) and computed their models with three different Z and Y values ([]0.03791, 0.30586]; [0.03837, 0.30655]; [0.03883, 0.30725]). We used a cost function (Eqn. 7) to investigate the age where the density, luminosity, $T_{\rm eff}$ and radius most closely matched that of the accretor. The ages for the models were between 0.63 and 0.69 Gy.

$$\text{Cost Function} = (L_E - L_B)^2/{L_{Berr}}^2 + (T_E - T_B)^2/{T_{Berr}}^2 + (R_E - R_B)^2/{R_{Berr}}^2 + (\rho_E - \rho_B)^2/{\rho_{Berr}}^2) \quad (7)$$

The following abbreviations are used: L, T, R and ρ stand for log($L/L_\odot$), $T_{\rm eff}$, R ($R_\odot$) and density (g cm^{-3}). E is the evolutionary model and B and Berr are the accretor model parameters and their uncertainties.

In subsection 3.1, we determined the average density of RZ Mic as 0.213 ± 0.006 g cm^{-3} which gave a 2.9% uncertainty, corresponding to a 1.5% uncertainty in the large separation, $\Delta\nu$. The MESA model with the closest density (0.219 g cm^{-3}) and lowest cost function, was from a mass of 2.0 $M_\odot$; Z= 0.0388; Y =0.3073 ([Fe/H] = 0.476); age = 0.672 Gyr. This model matched the accretor parameters within uncertainties as shown in Table 5. We used this model to calculate simple linear adiabatic frequencies with GYRE 5.2 , using the Magnus Multiple Shooting numerical scheme (Townsend & Teitler 2013; Townsend et al. 2018).

The rotation rate was set equal to the orbital period of the binary at 1.862 x 10^{-5} rad s^{-1}, as validated in Sections 3 and 5.1.

For these calculations, we used density to four decimal places as the MESA models were extremely sensitive to age and radius, and hence density. The large separation, $\Delta\nu$, was calculated from the average spacing of theoretical frequencies for the radial mode, $l = 0$ from GYRE, giving $\Delta\nu = 4.1$ d^{-1}, with a 1.1% uncertainty. We compared our $\Delta\nu$ and mean density for the RZ Mic accretor, to the scaling relation given in García Hernández et al. (2015, 2017) for δ Sct stars (Eqn. 8). This is a relationship between the stellar mean density and a frequency pattern, analogous to the solar-like large separation but offset by a constant of 1.55.

$$\frac{\bar{\rho}}{\bar{\rho}_\odot} = 1.50\left(\frac{\Delta\nu}{\Delta\nu_\odot}\right)^{2.04}, \quad (8)$$

where $\bar{\rho}$ is the mean density of the accretor in solar units, and $\Delta\nu_\odot = 134.8\,\mu$Hz.

This relationship, would require a much lower $\Delta\nu$ of ≈ 2, to match the mean density for the accretor in RZ Mic. This is significantly beyond the uncertainty for $\Delta\nu$ given by our density for the accretor, suggesting that this relationship does not apply to the RZ Mic accretor.

All predicted modes from GYRE indicated in Fig. 11 showed positive growth rates (η), albeit just positive with $\eta < 0.2$. This indicated that the modes were driven and may reach observable amplitude. Figure 11 shows these theoretical modes compared to the observed frequencies from *TESS* data.

Figure 11 has several striking features. Firstly, the $l = 0$, frequencies followed the typical pattern for non-linear pressure modes, where the lower frequencies showed a decrease in $\Delta\nu$. We investigated a smaller $\Delta\nu$ (3.8 d^{-1}) which had a similar effect. In comparison, the low-order, non-radial modes were misaligned and had the distinct signature of mixed modes. The latter exhibit gravity modes in the core which are able to cross the thin evanescent region, exhibiting pressure - mode characteristics in the envelope. This occurs when the p and g modes attain similar, but never exactly the same frequencies, as the star evolves with the convective core shrinking and the envelope expanding. Correspondingly, the g modes increase in frequency and the p modes decrease in frequency.

The dominant observed frequency, f_1, at 13.522 d^{-1}, was identified as one of these mixed modes at $n = 1$, $l = 1$, $m = -1$, a retrograde mode (refer to Table 6). This dipole mode originated as a g_1 mode, frequency = 12.167 d^{-1}, and was bumped into the pressure domain. This frequency is dependent on the size of the convective core and the treatment of convective-core overshooting (Dziembowski & Pamyatnykh 1991). The single-star model used for the GYRE calculations had a convective-core radius of 0.22 $R_\odot$. We also confirmed that f_1 fits the linear relationship between the frequency at maximum power and effective temperature as described by Forteza et al. (2018, 2020).

Secondly, f_2, at 25.619 d^{-1}, and f_3, at 20.279 d^{-1} were clearly not mixed modes. f_3 was also an $l = 1$ mode as was f_1, but of slightly higher radial order, $n = 3$, and is a prograde mode, $m = 1$. Both $l = 1$, $m = \pm 1$ are predicted to be visible at the inclination of RZ Mic, as is f_2, an $n = 4$, $l = 2$, $m = -2$ mode (Gizon & Solanki 2003). The observed frequencies with amplitudes < 0.1 mmag, were not considered sufficiently reliable for mode identification.

Mode identification for all three frequencies with < 0.5 % uncertainty strongly suggested that our prescription for convective-core overshooting in our evolutionary model was indeed correct. Indeed, modifying each frequency by its uncertainty does not result in a different identification.

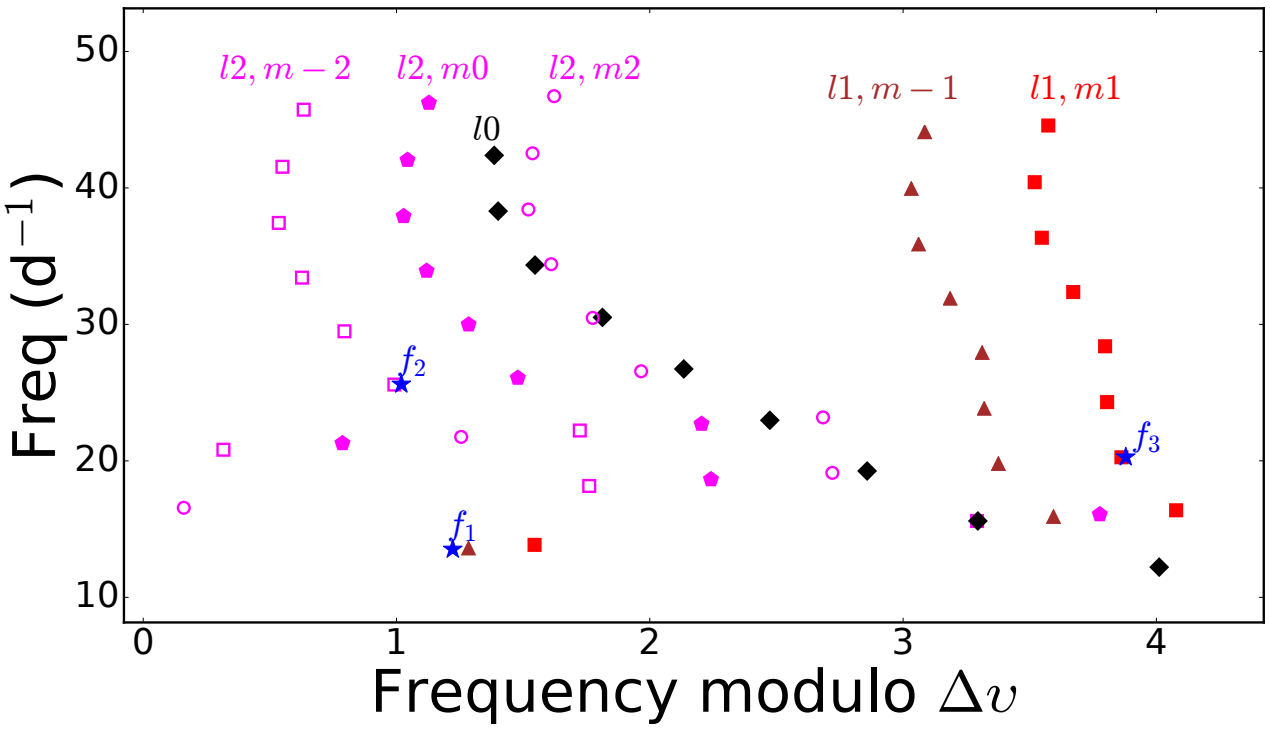

Figure 11. Echelle diagram showing calculated frequencies from GYRE compared to the observed frequencies from *TESS* data (blue stars). The input model for these calculations were for mass = 2.0 $M_\odot$; Z= 0.0388; Y =0.3073; age = 0.672 Gyr; density = 0.2193 g cm^3. Positive m values are prograde modes travelling in the direction of rotation. The large separation, $\Delta\nu$, was 4.1 d^{-1}. The highest radial order shown for each plot is $n = 10$.

7 SUMMARY AND CONCLUSIONS

Our initial aim was to identify the modes of the observed frequencies in the RZ Mic system. Modelling the combined photometry and spectroscopy data gave accurate fundamental parameters for the system and both components, all of which were crucial for this success. Additionally, *TESS* data were critical for definitive characterisation of the observed frequencies, as our ground data lacked continuity and time-coverage.

We determined that RZ Mic was a semi-detached, Algol-type system with a δ Sct primary component with fundamental parameters of $2.18 \pm 0.10\,M_\odot$, $2.43 \pm 0.05\,R_\odot$ and $T_{\rm eff} = 7300^{+200}_{-100}$ K. The companion star was a sub-giant which had filled its Roche lobe and donated mass to the δ Sct star. After subtraction of the binary models from the observed light curves, frequency analysis of the residual pulsations indicated one primary frequency ($f_1 = 13.522$ d^{-1}) and two of much lower amplitudes. Contrary to our expectations, *TESS* data revealed a similar number of frequencies as our ground data, with only four additional frequencies with amplitudes < 1 mmag.

We investigated evolutionary modelling of both the binary system and a single star but all resulted in higher temperatures (> 9000 K) and smaller radii ($< 1.8\,R_\odot$) for the pulsator compared to those given by the binary model. We investigated several possible causes for this, including overshooting of convective zones and the mixing length parameter. We only matched the temperature and radius of the pulsator by increasing the metallicity from solar and reducing the mass of the stellar model to the lower uncertainty of the pulsator mass. Our investigations highlighted the need for improved theoretical methods to explain chemical element transport for δ Sct stars.

The dominant frequency, f_1, in RZ Mic was a rotationally-split, dipole, mixed mode, $n_{\rm p} = 1$, $l = 1$, $m = -1$, from which we determined the convective-core radius as 0.22 R$_\odot$. The lowest amplitude frequency, f_3 is a prograde dipole mode. The f_2 frequency, was also rotationally-split and a retrograde quadrupole mode.

Given the short orbital period (≈ 4 d) and total mass $< 3\,M_\odot$ the RZ Mic system was almost certainly tidally-locked. This provided the rotation rate for an equivalent single-star evolutionary model to a certainty not given by other methods. Additionally, our binary model gave the density of the pulsator to a 2.9 % uncertainty. These two constraints were crucial for successful mode identification for the pulsator in RZ Mic. Therefore, determining the fundamental parameters of tidally-locked binary systems to the same levels of uncertainties is a plausible approach for identifying the pulsation modes of δ Sct stars.

While the evolution of a single star was quite different to that of the pulsator in RZ Mic, because of the mass gain of the latter, their fundamental parameters were equivalent. The reverse approach is feasible if a suitable number of close binaries has been modelled. If the frequency pat-

tern of a single star matches that of a binary pulsator then the fundamental parameters of the single star together with its rotation velocity can be deduced. This would only apply to a cohort of single stars with the low rotational velocities ($\leq 50\,\mathrm{km\,s^{-1}}$) seen in close binary systems. This future application would be facilitated using a combination of the frequency spectrum with Gaia distance and projected rotational velocity.

ACKNOWLEDGEMENTS

This project made use of the following software: PHOEBE2 (Horvat et al. 2018, 2019), EMCEE (Foreman-Mackey et al. 2013), Period04 (Lenz & Breger 2005), MESA (Paxton et al. 2011, 2013, 2015, 2018, 2019), GYRE (Townsend & Teitler 2013; Townsend et al. 2018); Python: numpy (Oliphant 2006), matplotlib (Hunter 2007), scypy (Virtanen et al. 2020),

This research is supported by an Australian Government Research Training Program (RTP) Scholarship (MS). MJ was supported by the Research School of Astronomy and Astrophysics at the Australian National University and funding from Australian Research Council grant No. DP150100250. MJ further acknowledges the University of Sydney for academic and resource support as well as the MESA and GYRE developers for their maintenance of these tools. SJM is the recipient of an Australian Research Council Discovery Early Career Award (project number 180101104), funded by the Australian Government. MŽ acknowledges funding from the Australian Research Council (grant DP170102233). This paper includes data collected by the TESS mission. Funding for the TESS mission is provided by the NASA Explorer Program. This research was made possible through the use of the AAVSO Photometric All-Sky Survey (APASS), funded by the Robert Martin Ayers Sciences Fund. The Digitized Sky Surveys were produced at the Space Telescope Science Institute under U.S. Government grant NAG W-2166. The images of these surveys are based on photographic data obtained using the Oschin Schmidt Telescope on Palomar Mountain and the UK Schmidt Telescope. The plates were processed into the present compressed digital form with the permission of these institutions. This publication makes use of data products from the Two Micron All Sky Survey, which is a joint project of the University of Massachusetts and the Infrared Processing and Analysis Center/California Institute of Technology, funded by the National Aeronautics and Space Administration and the National Science Foundation. This work has made use of data from the European Space Agency (ESA) mission *Gaia* (https://www.cosmos.esa.int/gaia), processed by the *Gaia* Data Processing and Analysis Consortium (DPAC, https://www.cosmos.esa.int/web/gaia/dpac/consortium). Funding for the DPAC has been provided by national institutions, in particular the institutions participating in the *Gaia* Multilateral Agreement. This work makes use of observations from the LCOGT network.

DATA AVAILABILITY

The ground-based photometry data from the Murrumbateman site are available from the AAVSO site: https://www.aavso.org/.

The *TESS* data for RZ Mic are available at: https://mast.stsci.edu/portal/Mashup/Clients/Mast/Portal.html.

REFERENCES

Aerts C., 2019, arXiv:1912.12300 [astro-ph]
Aerts C., Christensen-Dalsgaard J., Kurtz D. W., 2010, Asteroseismology. http://adsabs.harvard.edu/abs/2010aste.book.....A
Andrae R., et al., 2018, Astronomy and Astrophysics, 616, A8
Antoci V., et al., 2014, The Astrophysical Journal, 796, 118
Antoci V., et al., 2019, Mon Not R Astron Soc, 490, 4040
Asplund M., Grevesse N., Sauval A. J., Scott P., 2009, Annual Review of Astronomy and Astrophysics, 47, 481
Auvergne M., et al., 2009, Astronomy and Astrophysics, 506, 411
Balona L. A., Dziembowski W. A., 2011, Monthly Notices of the Royal Astronomical Society, 417, 591
Bedding T. R., 2014, in , Asteroseismology. p. 60, http://adsabs.harvard.edu/abs/2014aste.book...60B
Bedding T. R., et al., 2020, Nature, 581, 147
Borucki W. J., et al., 2010, Science, 327, 977
Bowman D. M., Kurtz D. W., 2018, Mon Not R Astron Soc, 476, 3169
Bowman D. M., Kurtz D. W., Breger M., Murphy S. J., Holdsworth D. L., 2016, Monthly Notices of the Royal Astronomical Society, 460, 1970
Breger M., Bregman J. N., 1975, The Astrophysical Journal, 200, 343
Castelli F., Kurucz R. L., 2004, ArXiv Astrophysics e-prints, pp arXiv:astro–ph/0405087
Chen X., Maxted P. F. L., Li J., Han Z., 2017, Mon Not R Astron Soc, 467, 1874
Chen X., Li Y., Zhang X., 2019, The Astrophysical Journal, 887, 253
Childress M. J., Vogt F. P. A., Nielsen J., Sharp R. G., 2014, Astrophysics and Space Science, 349, 617
Choi J., Dotter A., Conroy C., Cantiello M., Paxton B., Johnson B. D., 2016, The Astrophysical Journal, 823, 102
Collaboration T. A., et al., 2018, AJ, 156, 123
Deal M., Goupil M.-J., Marques J. P., Reese D. R., Lebreton Y., 2020, A&A, 633, A23
Dopita M., Hart J., McGregor P., Oates P., Bloxham G., Jones D., 2007, Astrophysics and Space Science, 310, 255
Dopita M., et al., 2010, Astrophysics and Space Science, 327, 245
Dotter A., 2016, The Astrophysical Journal Supplement Series, 222, 8
Dupret M. A., et al., 2009, A&A, 506, 57
Dziembowski W. A., Pamyatnykh A. A., 1991, Astronomy and Astrophysics, 248, L11
Foreman-Mackey D., Hogg D. W., Lang D., Goodman J., 2013, Publications of the Astronomical Society of the Pacific, 125, 306
Forteza S. B., Cortés T. R., García R. A., 2018, A&A, 614, A46
Forteza S. B., Moya A., Barrado D., Solano E., Martín-Ruiz S., Suárez J. C., Hernández A. G., 2020, A&A, 638, A59
Fuller J., 2017, Monthly Notices of the Royal Astronomical Society, 472, 1538
García Hernández A., Martín-Ruiz S., Monteiro M. J. P. F. G., Suárez J. C., Reese D. R., Pascual-Granado J., Garrido R., 2015, The Astrophysical Journal, 811, L29

García Hernández A., et al., 2017, Mon Not R Astron Soc Lett, 471, L140
Garrido R., Garcia-Lobo E., Rodriguez E., 1990, Astronomy and Astrophysics, 234, 262
Gizon L., Solanki S. K., 2003, The Astrophysical Journal, 589, 1009
Grigahcène A., et al., 2010, The Astrophysical Journal Letters, 713, L192
Guo Z., Fuller J., Shporer A., Li G., Hambleton K., Manuel J., Murphy S., Isaacson H., 2019, ApJ, 885, 46
Hambleton K., et al., 2017, arXiv:1706.05051 [astro-ph]
Handler G., et al., 2020, Nature Astronomy, 4, 684
Hauschildt P. H., Allard F., Baron E., 1999a, The Astrophysical Journal, 512, 377
Hauschildt P. H., Allard F., Ferguson J., Baron E., Alexander D. R., 1999b, The Astrophysical Journal, 525, 871
Henyey L., Vardya M. S., Bodenheimer P., 1965, The Astrophysical Journal, 142, 841
Hoffmeister C., 1956, Veroeffentlichungen der Sternwarte Sonneberg, 3, 1
Horvat M., Conroy K. E., Pablo H., Hambleton K. M., Kochoska A., Giammarco J., Prša A., 2018, The Astrophysical Journal Supplement Series, 237, 26
Horvat M., Conroy K. E., Jones D., Prša A., 2019, The Astrophysical Journal Supplement Series, 240, 36
Hunter J. D., 2007, Computing in Science & Engineering, 9, 90
Hurley J. R., Tout C. A., Pols O. R., 2002, Monthly Notices of the Royal Astronomical Society, 329, 897
Iglesias C. A., Rogers F. J., 1996, The Astrophysical Journal, 464, 943
Joyce M., Chaboyer B., 2018, The Astrophysical Journal, 856, 10
Kahraman Aliçavuş F., Soydugan E., Smalley B., Kubát J., 2017, Mon Not R Astron Soc, 470, 915
Kaye A. B., Handler G., Krisciunas K., Poretti E., Zerbi F. M., 1999, Publications of the Astronomical Society of the Pacific, 111, 840
Kjeldsen H., Bedding T. R., 1995, Astronomy and Astrophysics, 293, 87
Kolb U., Ritter H., 1990, Astronomy and Astrophysics, 236, 385
Kurtz D. W., et al., 2020, MNRAS, 494, 5118
Landolt A. U., 2007, The Astronomical Journal, 133, 2502
Ledoux P., 1947, The Astrophysical Journal, 105, 305
Lee J. W., Kristiansen M. H., Hong K., 2019, The Astronomical Journal, 157, 223
Lenz P., Breger M., 2005, Communications in Asteroseismology, 146, 53
Li T., Bedding T. R., Huber D., Ball W. H., Stello D., Murphy S. J., Bland-Hawthorn J., 2018, Monthly Notices of the Royal Astronomical Society, 475, 981
Liakos A., Niarchos P., 2017, Monthly Notices of the Royal Astronomical Society, 465, 1181
Lucy L. B., 1967, Zeitschrift fur Astrophysik, 65, 89
Magic Z., Collet R., Asplund M., Trampedach R., Hayek W., Chiavassa A., Stein R. F., Nordlund Å., 2013, Astronomy and Astrophysics, 557, A26
Murphy S. J., Bedding T. R., Shibahashi H., Kurtz D. W., Kjeldsen H., 2014, Monthly Notices of the Royal Astronomical Society, 441, 2515
Murphy S. J., Hey D., Van Reeth T., Bedding T. R., 2019, Mon Not R Astron Soc, 485, 2380
Norris J. E., et al., 2013, The Astrophysical Journal, 762, 25
Oliphant T. E., 2006, A guide to NumPy. Vol. 1, Trelgol Publishing USA
Pamyatnykh A. A., 2000, in Breger M., Montgomery M., eds, Astronomical Society of the Pacific Conference Series Vol. 210, Delta Scuti and Related Stars. p. 215 (arXiv:astro-ph/0005276)
Paxton B., Bildsten L., Dotter A., Herwig F., Lesaffre P., Timmes F., 2011, ApJS, 192, 3
Paxton B., et al., 2013, ApJS, 208, 4
Paxton B., et al., 2015, The Astrophysical Journal Supplement Series, 220, 15
Paxton B., et al., 2018, The Astrophysical Journal Supplement Series, 234, 34
Paxton B., et al., 2019, The Astrophysical Journal Supplement Series, 243, 10
Prša A., 2018, Modeling and Analysis of Eclipsing Binary Stars. 2514-3433, IOP Publishing, doi:10.1088/978-0-7503-1287-5, http://dx.doi.org/10.1088/978-0-7503-1287-5
Prša A., et al., 2016, The Astrophysical Journal Supplement Series, 227, 29
Ricker G. R., et al., 2015, Journal of Astronomical Telescopes, Instruments, and Systems, 1, 014003
Robitaille T. P., et al., 2013, A&A, 558, A33
Rossiter R. A., 1924, The Astrophysical Journal, 60
Schlafly E. F., Finkbeiner D. P., 2011, The Astrophysical Journal, 737, 103
Schmid V. S., Aerts C., 2016, Astronomy & Astrophysics, 592, A116
Skrutskie M. F., et al., 2006, The Astronomical Journal, 131, 1163
Smalley B., et al., 2017, Monthly Notices of the Royal Astronomical Society, 465, 2662
Streamer M., Bohlsen T., Ogmen Y., 2016, Journal of the American Association of Variable Star Observers (JAAVSO), 44, 39
Streamer M., Ireland M. J., Murphy S. J., Bento J., 2018, Mon Not R Astron Soc, 480, 1372
Tayar J., et al., 2017, The Astrophysical Journal, 840, 17
Tkachenko A., et al., 2020, A&A, 637, A60
Torres G., Andersen J., Giménez A., 2010, Astron Astrophys Rev, 18, 67
Townsend R. H. D., Teitler S. A., 2013, Monthly Notices of the Royal Astronomical Society, 435, 3406
Townsend R. H. D., Goldstein J., Zweibel E. G., 2018, Mon Not R Astron Soc, 475, 879
Virtanen P., et al., 2020, Nature Methods, 17, 261
Wilson R. E., Devinney E. J., 1971, The Astrophysical Journal, 166, 605
Yang T.-Z., Liu J., Zuo Z., 2019, arXiv e-prints, 1912, arXiv:1912.04167
Ziaali E., Bedding T. R., Murphy S. J., Van Reeth T., Hey D. R., 2019, Mon Not R Astron Soc, 486, 4348
Zorec J., Royer F., 2012, Astronomy and Astrophysics, 537, A120
Zucker S., Mazeh T., 1994, The Astrophysical Journal, 420, 806

This paper has been typeset from a TEX/LATEX file prepared by the author.